Dark matter-induced electron excitations in silicon and germanium with deep learning

Letter

Dark matter-induced electron excitations in silicon and germanium with deep learning

Riccardo Catena* and Einar Urdshals†

Chalmers University of Technology, Department of Physics, SE-412 96 Göteborg, Sweden

(Received 12 April 2024; accepted 13 December 2024; published 14 January 2025)

We train a deep neural network (DNN) to output rates of dark matter (DM) induced electron excitations in silicon and germanium detectors. Our DNN provides a massive speedup of around 5 orders of magnitude relative to existing methods (i.e., QEdark-EFT), allowing for extensive parameter scans in the event of an observed DM signal. The network is also lighter and simpler to use than alternative computational frameworks based on a direct calculation of the DM-induced excitation rate.

DOI: 10.1103/PhysRevD.111.L011702

Introduction. Learning the nature of dark matter (DM) is a key challenge in modern astroparticle physics. It is known to exist from its gravitational influence on the visible Universe, and plays a crucial role in a multitude of phenomena across vastly different astrophysical scales [1].

On cosmological scales, DM initiates the formation of large scale structures, giving rise to galaxies and galaxy clusters. It also generates the density fluctuations leading to the observed patterns of anisotropy in the cosmic microwave background temperature and polarization maps [2]. On galactic scales, the influence of DM is visible through gravitational lensing [3], and the flattening of rotation curves in spiral galaxies [4].

Despite the crucial role of DM in explaining these phenomena, its nature is yet to be determined. The leading hypothesis in the field of astroparticle physics is that DM is made up of new particles, waiting to be discovered [1]. The identity and properties of these particles do however still remain to be determined.

The strong gravitational evidence for the presence of large amounts of DM in the Universe contrasts with the lack of a microscopic description for this invisible and unidentified cosmic component. This contrast makes the pursuit of the nature of DM a key focus in the present scientific research. There are several kinds of experiments searching to unveil the nature of DM. An important family relies on the direct detection technique [5,6]. These experiments seek to observe rare interactions between DM particles from the Milky Way and detector materials placed deep underground in low-background environments.

Traditionally, direct detection experiments have primarily focused on searching for nuclear recoil events induced by weakly interacting massive particles scattering off target nuclei in crystals or liquid noble gases [7]. As a result, these experiments have mainly been sensitive to DM masses in the GeV–TeV range, as lighter particles would be unable to generate observable nuclear recoils.

With the absence of direct evidence for weakly interacting massive particles, efforts have been put in towards alternative experimental approaches better suited to probe DM particles with sub-GeV masses [8]. In this context, a crucial role is played by direct detection experiments designed to detect DM-induced electronic transitions or electron ejections in materials, offering a novel avenue for uncovering the nature of DM [9–20].

To interpret these experiments, a theoretical understanding of DM-electron interactions in detector materials is needed. In Refs. [21–25], the interactions DM can have with the electrons bound to silicon and germanium crystals (as well as individual atoms and graphene targets) were classified and explored using a nonrelativistic effective theory formalism. We implemented our formalism in QEdark-EFT [26], which interfaces with the plane-wave self-consistent field Density Functional Theory (DFT) code Quantum ESPRESSO [27] and extends the QEdark code [28] to the case of general DM-electron interactions. This allowed for covering several DM models, although an extensive exploration was hindered by computational costs.

The deep neural network (DNN) developed in this paper is trained on the output of QEdark-EFT and serves mainly two purposes. First, it is easier to use and run than QEdark-EFT. It takes less space on a hard drive and does not require computation of or access to material response functions. Second, it allows for evaluating a large number of DM-induced electronic transition rates cheaply on a laptop,

*Contact author: catena@chalmers.se
†Contact author: urdshals@chalmers.se

and demonstrates the potential DNNs have for speeding up rate evaluations. Such a speedup will be necessary to perform extensive parameter scans in the event of detection of a DM signal. For example, evaluating the rate of electron-hole pair creation in silicon and germanium for 10^6 DM models takes 30 s with our DNN, compared to days with QEdark-EFT.

This work is organized as follows. In the next section, we review the theory of DM-electron scattering in materials, focusing on the effective theory approach of Ref. [22]. Following that, we introduce our DNN structure and training strategy. Finally, we report the results we find when testing the accuracy of our DNN in our third section and then conclude.

DM-induced electron excitations in crystals. The rate at which DM events occur creating i electron hole pairs in crystals is given as [22]

$$\mathcal{R}_i = \frac{n_\chi N_{\rm cell}}{128\pi m_\chi^2 m_e^2} \int_{E_{\rm gap}+(i-1)\varepsilon}^{E_{\rm gap}+i\varepsilon} {\rm d}(\ln \Delta E) \int {\rm d}q\, q \hat{\eta}(q,\Delta E) \times \sum_{l=1}^{5} \Re\left(R_l^*(q,v)\bar{W}_l(q,\Delta E)\right), \quad (1)$$

where n_χ is the number density of DM particles, m_χ and m_e are the mass of the DM particle and the electron, $N_{\rm cell}$ is the number of unit cells in the crystal and ΔE and q are the energy and momentum that the DM particle deposits to the crystal. $\hat{\eta}(q,\Delta E)$ denotes the velocity integral [22], which is performed using the Standard Halo Model (SHM) with $v_0 = 238$ km/s, $v_e = 250.5$ km/s, and $v_{\rm esc} = 544$ km/s [29]. R_l and $\bar{W}_l$ are the DM and material response function [22]. We calculate the latter within DFT, using the `Si.pbe-n-rrkjus_psl.0.1.UPF` pseudopotential for silicon and the `Ge.pbe-dn-rrkjus_psl.0.2.2.UPF` pseudopotential for germanium. These are provided with Quantum ESPRESSO, and include the $3s^2$, $3p^2$ electrons for silicon, and the $4s^2$, $4p^2$, and $3d^{10}$ electrons for germanium in the valence configuration. For the treatment of electron-electron exchange and correlation we use the PBE functional, and sample reciprocal space using a $6\times6\times6$ Monkhorst-Pack k-point grid. Following Ref. [28], we supplement this sampling with additional k points at and close to Γ and half way to the zone boundary. We perform our calculations at the experimental value of the lattice constants $a_{\rm Si} = 10.3305$ a.u. and $a_{\rm Ge} = 10.8171$ a.u., and take an energy cutoff $E_{\rm cut} = 120$ Ry (1.6 keV) for silicon and $E_{\rm cut} = 100$ Ry (1.4 keV) for germanium. Furthermore, we apply a Hubbard U correction with a value of $U_{\rm eff} = 9.45$ eV to the Ge $3d$ orbitals, which has the effect of shifting the Ge $3d$ band down in energy by approximately $U_{\rm eff}/2$, so that its position below the Fermi level is consistent with experimental observations. Finally, we use a scissors correction to set the band gap of silicon (germanium) to the experimental value of 1.2 eV (0.67 eV). The energy required to create an additional electron hole pair ε and the band gap $E_{\rm gap}$ depend on the material and are given by [30,31]

$$\begin{aligned} \varepsilon &= 3.8\ {\rm eV} && \text{silicon} \\ \varepsilon &= 3.0\ {\rm eV} && \text{germanium} \\ E_{\rm gap} &= 1.2\ {\rm eV} && \text{silicon} \\ E_{\rm gap} &= 0.67\ {\rm eV} && \text{germanium.} \end{aligned}$$

For fixed material properties and DM velocity distribution, the observable quantity $\mathcal{R}_i$ is a unique function of the m_χ and the DM response function. The DM response function is in turn specified by the nonrelativistic effective theory couplings. We follow Ref. [22], and expand the matrix element—from which the DM and material response functions arise—in nonrelativistic effective operators as

$$\mathcal{M}(\mathbf{q},\mathbf{v}_{\rm el}^\perp) = \sum_j \left(c_j^s + c_j^\ell \frac{q_{\rm ref}^2}{|\mathbf{q}|^2}\right)\langle \mathcal{O}_i\rangle, \quad (2)$$

and consider only DM models in which the mediator mass is either much smaller than the typical momentum transfer, $q_{\rm ref} = \alpha m_e$, or much larger than $q_{\rm ref}$. We refer to these two cases as "long range" and "short range" interactions, respectively. We denote by c_j^ℓ and c_j^s the corresponding couplings, and use the index j to label the operator type. As shown in [21], if DM has spin 0 or 1/2 there are 14 such effective theory couplings for every mediator mass scenario. The associated operators are listed in Table I. Note that these operators contain different powers of $q/m_e \sim \alpha = 1/137$ and $v_{\rm el}^\perp \sim 10^{-3}$. This leads to different levels of suppression for the different operators, namely

TABLE I. Interaction operators defining the nonrelativistic effective theory of spin 0 or spin 1/2 DM-electron interactions [21,32,33]. $\mathbf{S}_e$ ($\mathbf{S}_\chi$) is the electron (DM) spin, while $\mathbf{v}_{\rm el}^\perp = \mathbf{v} - \boldsymbol{\ell}/m_e - \mathbf{q}/(2\mu_{\chi e})$ is the transverse DM-electron relative velocity (in the limit of elastic interactions). Here, $\mu_{\chi e}$ is the DM-electron reduced mass, $\mathbf{v}$ is the incoming DM particle velocity, $\boldsymbol{\ell}$ is the initial electron momentum, m_e is the electron mass, and $\mathbb{1}_{\chi e}$ is the identity in the DM-electron spin space.

$\mathcal{O}_1 = \mathbb{1}_{\chi e}$	$\mathcal{O}_9 = i\mathbf{S}_\chi \cdot (\mathbf{S}_e \times \frac{\mathbf{q}}{m_e})$
$\mathcal{O}_3 = i\mathbf{S}_e \cdot (\frac{\mathbf{q}}{m_e} \times \mathbf{v}_{\rm el}^\perp)$	$\mathcal{O}_{10} = i\mathbf{S}_e \cdot \frac{\mathbf{q}}{m_e}$
$\mathcal{O}_4 = \mathbf{S}_\chi \cdot \mathbf{S}_e$	$\mathcal{O}_{11} = i\mathbf{S}_\chi \cdot \frac{\mathbf{q}}{m_e}$
$\mathcal{O}_5 = i\mathbf{S}_\chi \cdot (\frac{\mathbf{q}}{m_e} \times \mathbf{v}_{\rm el}^\perp)$	$\mathcal{O}_{12} = \mathbf{S}_\chi \cdot (\mathbf{S}_e \times \mathbf{v}_{\rm el}^\perp)$
$\mathcal{O}_6 = (\mathbf{S}_\chi \cdot \frac{\mathbf{q}}{m_e})(\mathbf{S}_e \cdot \frac{\mathbf{q}}{m_e})$	$\mathcal{O}_{13} = i(\mathbf{S}_\chi \cdot \mathbf{v}_{\rm el}^\perp)(\mathbf{S}_e \cdot \frac{\mathbf{q}}{m_e})$
$\mathcal{O}_7 = \mathbf{S}_e \cdot \mathbf{v}_{\rm el}^\perp$	$\mathcal{O}_{14} = i(\mathbf{S}_\chi \cdot \frac{\mathbf{q}}{m_e})(\mathbf{S}_e \cdot \mathbf{v}_{\rm el}^\perp)$
$\mathcal{O}_8 = \mathbf{S}_\chi \cdot \mathbf{v}_{\rm el}^\perp$	$\mathcal{O}_{15} = i\mathcal{O}_{11}[(\mathbf{S}_e \times \mathbf{v}_{\rm el}^\perp) \cdot \frac{\mathbf{q}}{m_e}]$

Operators	Suppression parameter S_j
$\mathcal{O}_1, \mathcal{O}_4$	$(v_{\rm el}^{\perp})^0 (q/m_e)^0$
$\mathcal{O}_9, \mathcal{O}_{10}, \mathcal{O}_{11}$	$(v_{\rm el}^{\perp})^0 (q/m_e)^1$
$\mathcal{O}_7, \mathcal{O}_8, \mathcal{O}_{12}$	$(v_{\rm el}^{\perp})^1 (q/m_e)^0$
$\mathcal{O}_6$	$(v_{\rm el}^{\perp})^0 (q/m_e)^2$
$\mathcal{O}_3, \mathcal{O}_5, \mathcal{O}_{13}, \mathcal{O}_{14}$	$(v_{\rm el}^{\perp})^1 (q/m_e)^1$
$\mathcal{O}_{15}$	$(v_{\rm el}^{\perp})^1 (q/m_e)^2$.

(3)

When using the suppression parameter S_j to rescale the couplings as explained below in Sec. II, we set $q/m_e = 1/137$ and $v_{\rm el}^{\perp} = 10^{-3}$.

The observable $\mathcal{R}_i$ is thus uniquely determined by 29 real parameters. This problem is well suited to emulate with a feed forward neural network taking the 29 model parameters as input and outputting $\mathcal{R}_i$ for the n most relevant values of i. We restrict ourselves to consider i ranging from 1 to $n = 4$, as these rate bins dominate for the DM masses considered here.

$\mathcal{R}_i$ varies over several orders of magnitude depending on m_χ and the effective theory couplings. Rather than outputting $\mathcal{R}_i$ directly, we find it beneficial to output s and $\mathcal{R}'_i$ defined as

$$s = \frac{\sum_i^n \ln(\mathcal{R}_i)}{n}, \tag{4}$$

$$\mathcal{R}'_i = \ln(\mathcal{R}_i) - s. \tag{5}$$

Here, s sets the overall scale of the rate, whereas $\mathcal{R}'_i$ gives the shape of the spectrum. This distinction allows the network to learn the shape given by $\mathcal{R}'_i$, and the overall scale of the rate set by s separately. Furthermore, to avoid terms in Eq. (5) diverging, we consider only values of m_χ for which $\mathcal{R}_i$ is nonzero for all i. To avoid parameter space with $\mathcal{R}_i = 0$, we only consider

$$m_\chi > 2\frac{E_{\rm gap} + \varepsilon(n-1)}{(v_e + v_{\rm esc})^2}, \tag{6}$$

where $v_e + v_{\rm esc} = 788$ km/s [29] is the maximal speed of Milky Way bound DM particle seen from Earth. For $n = 4$ and the properties of silicon and germanium we include DM masses

$$\begin{aligned} &4\ \text{MeV} \le m_\chi \le 1\ \text{GeV} \qquad \text{silicon}, \\ &3\ \text{MeV} \le m_\chi \le 1\ \text{GeV} \qquad \text{germanium}. \end{aligned} \tag{7}$$

As such, the DNN has 29 real scalars as input and 5 real scalars as output.

DNN structure and training. We use a feed forward neural network with 29 neurons in the flattening input layer, followed by six dense layers with 64, 128, 128, 64, 32, 16 neurons, respectively, and finally a dense output layer with 5 neurons. This gives a total of 37,701 trainable parameters, and we use ReLu [34] as the activation function in all the hidden layers. We implement the DNN using TensorFlow [35], and train on two precomputed datasets of 4.2×10^6 combinations of m_χ and effective couplings, one for silicon and one for germanium. The training is performed using the Adam [36] optimizer and mean square error as loss function. The training loop shown in Fig. 1 is used to avoid overfitting, with the test datasets consisting of 1.4×10^6 combinations of m_χ and effective couplings. After training we evaluate the network on a third data set with 10^5 data points.

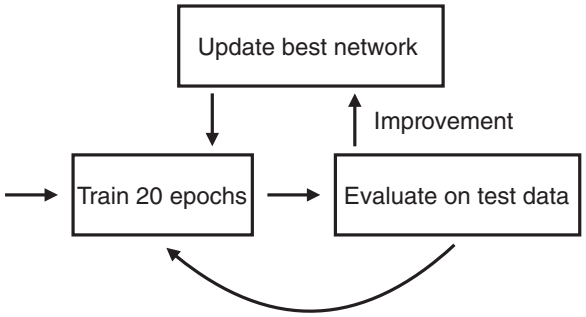

FIG. 1. Training loop designed to avoid overfitting. Every 20 epochs the performance of the network on the test data is evaluated, and the network configuration that performs the best on the test data is being updated and stored.

We generate the dataset by drawing m_χ from a log distribution in the range given in Eq. (7). We also set m effective couplings different from 0, where m is a random integer drawn from a uniform distribution between 1 and 28. We make it random which couplings are different from 0, and these are drawn from a uniform distribution between -1 and 1. Having drawn c_j^s, c_j^ℓ and m_χ, $\mathcal{R}_i$ is computed using the code we developed in Refs. [22,26], QEdark-EFT. During the computation, c_j^s and c_j^ℓ are adjusted upward by S_j^{-1} from Eq. (3). This is done to avoid $j = 1$ and $j = 4$ always dominating. Before training the neural network m_χ is transformed as

$$m_\chi \to \frac{-2}{\ln\left(\frac{m_{\rm min}}{1\ \text{GeV}}\right)} \ln\left(\frac{m_\chi}{1\ \text{GeV}}\right) + 1, \tag{8}$$

where $m_{\rm min} = 4$ MeV ($m_{\rm min} = 3$ MeV) is the minimal mass considered for Si (Ge). This is done to ensure that the mass parameter fed to the neural network approximately lies between -1 and 1.

To summarize, the DNN takes in 28 c_j^s or c_j^ℓ parameters between -1 and 1 together with a mass parameter between -1 and 1. The DNN outputs s and $\mathcal{R}'_i$ from Eq. (5), where $\mathcal{R}_i$ is the rate of electron hole pairs expected to be created by a DM model with couplings between $-S_j^{-1}$ and S_j^{-1} and a DM mass between 4 MeV (3 MeV) and 1 GeV for Si (Ge).

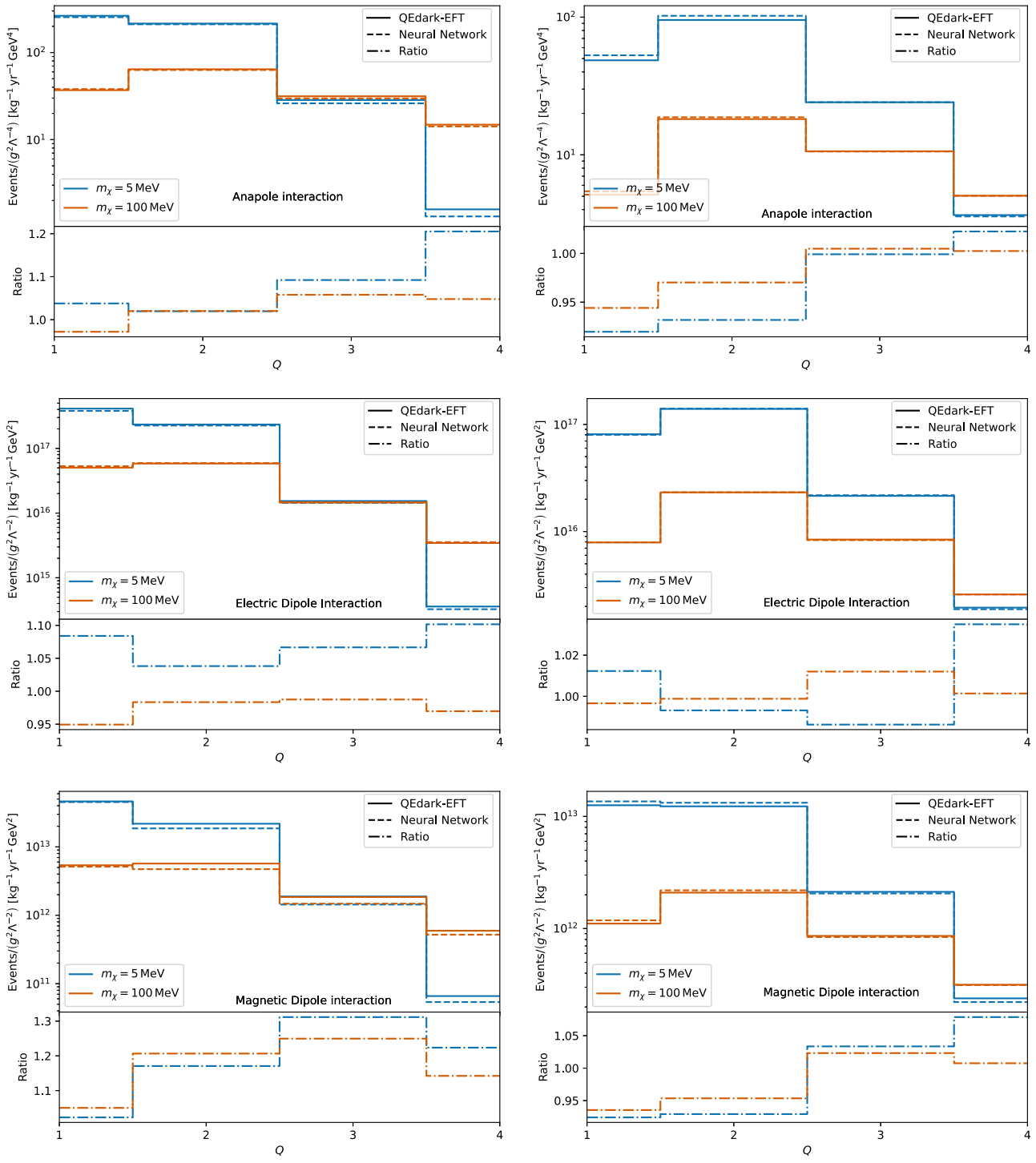

FIG. 2. Comparison between the excitation rates from Ref. [22] (solid lines) and the rates inferred here by the DNN (dashed lines). The panels to the left correspond to silicon, whereas the panels to the right correspond to germanium. The blue lines are for $m_\chi = 5$ MeV while the red lines are for $m_\chi = 100$ MeV. See legends, for further details about the assumed DM interaction.

Results. After training, the DNNs are evaluated on 10^5 data points in the validation set. These are generated in the same way as the training data, and the network reproduces these data points with an average relative error of around 2.76% (2.62%) for silicon (germanium). In order to test the accuracy of our DDN-based computational framework, in Fig. 2 we compare the electron-hole creation rate computed in Ref. [22] for anapole, electric dipole, and magnetic dipole interactions through a direct calculation with predictions obtained here using our DNN. These interactions

generate the following nonzero coupling constants [22]:

$$c_8^s = 8em_e m_\chi \frac{g}{\Lambda^2}, \tag{9a}$$

$$c_9^s = -8em_e m_\chi \frac{g}{\Lambda^2}, \tag{9b}$$

for the anapole interaction,

$$c_{11}^\ell = \frac{16em_\chi m_e^2}{q_{\rm ref}^2}\frac{g}{\Lambda}. \tag{10}$$

for the electric dipole interaction, and finally

$$c_1^s = 4em_e \frac{g}{\Lambda}, \tag{11a}$$

$$c_4^s = 16em_\chi \frac{g}{\Lambda}, \tag{11b}$$

$$c_5^\ell = \frac{16em_e^2 m_\chi}{q_{\rm ref}^2}\frac{g}{\Lambda}, \tag{11c}$$

$$c_6^\ell = -\frac{16em_e^2 m_\chi}{q_{\rm ref}^2}\frac{g}{\Lambda}, \tag{11d}$$

for the magnetic dipole interaction. We stress that the DNN has not been trained on these particular interactions. It is thus remarkable that our DNN reproduces the associated excitation rates with a good accuracy, as one can see from Fig. 2. The DNN predictions for magnetic dipole interactions in silicon exhibit the largest deviation from the actual excitation rate, this deviation being larger than 30% for $i = 3$ and $m_\chi = 5$ MeV. In all other cases, we find that our DNN reproduces the expected rates of electron-hole pair creation within an accuracy of about 10% or below. Finally, in a wide range of DM masses and interactions, the predictions of our DNN match the results obtained by an explicit rate calculation within an accuracy which is below 5%.

Focusing on the computational costs, we stress that generating excitation rates within our DNN-based computational framework is extremely fast. On the CPU of a laptop, generating 10^6 (10^7) rates takes roughly 30 seconds (300 seconds), showing that we are in a regime where the computation time is linear in the number of rate evaluations. This is five orders of magnitude faster than our code from Refs. [22,26], QEdark-EFT, which relies on precomputed and tabulated material response functions.

Summary and conclusion. We trained a feed forward DNN to generate rates of DM-induced electron excitations in silicon and germanium detectors as an output. We performed this training with TensorFlow [35] using the Adam [36] optimizer. Both for silicon and for germanium, we trained our DNN on precomputed training, test, and evaluation datasets of 4.2×10^6, 1.4×10^6, and 10^5 combinations of DM particle mass and effective couplings, respectively. The evaluation set was reproduced with an average relative error of around 2.79% (2.62%) for silicon (germanium). Focusing on anapole, electric and magnetic dipole DM interactions, we find that our DNN reproduces the expected rates of electron-hole pair creation within an accuracy of about 10% or below in a wide range of DM particle masses. In terms of computational costs, the improvement compared to existing computational frameworks is remarkable. Generating 10^6 excitation rates with our DNN takes roughly 30 seconds on the CPU of a laptop, and is thus five orders of magnitude faster than with QEdark-EFT [22,26], which relies on precomputed and tabulated material response functions. This massive speedup in the computing time allows us to perform extensive parameter scans, which are relevant both in the event of an observed DM signal and in the analysis of the null result reported by the operating experiments.

Our analysis serves as a proofs of concept and can be improved in different ways. In particular, since we use QEdark-EFT to generate the training data, the accuracy of our modeling of the DM-electron interaction is that of QEdark-EFT. A first improvement would be to include in-medium screening via the dielectric function in our rate calculations. Interestingly, an estimate of this effect could be performed within our DNN framework by realizing that (1) the imaginary part of the dielectric function is proportional to $\bar{W}_1$, and (2) the Kramers-Kronig relations can be used to obtain the real part of the dielectric function from its imaginary part. A second improvement would consist in training our DDN to emulate the transition rates in germanium detectors for events with a number of e-h pairs that is larger than four. This extension of our analysis is expected to be relevant in the case of DM candidates of mass larger than about 100 MeV [28]. Finally, our analysis could be further improved by refining the electron-hole pair production model we employ within our DNN framework, which is known to break down at low enough energies [37]. In the case of silicon, this could be done by implementing in the DNN training data the results of [37], where a ionization response model valid between 1.2 and 8 eV is reported.

Acknowledgments. It is a pleasure to thank Hanna Olvhammar for contributing to the early stages of this project. We are also grateful to Marek Matas and Nicola A. Spaldin for their contributions to the development of QEdark-EFT [26], which we extensively used in this work. R. C. acknowledges support from an individual research grant from the Swedish Research Council (Dnr. 2022-04299) and from the Knut and Alice Wallenberg Foundation project "Light Dark Matter" (Dnr. KAW 2019.0080).

Data availability. The DNN can be downloaded in Ref. [38].

[1] Gianfranco Bertone and Dan Hooper, History of dark matter, Rev. Mod. Phys. **90**, 045002 (2018).

[2] Nabila Aghanim *et al.* (Planck Collaboration), Planck 2018 results. VI. Cosmological parameters, Astron. Astrophys. **641**, A6 (2020); Astron. Astrophys. **652**, C4(E) (2021).

[3] Douglas Clowe, Marusa Bradac, Anthony H. Gonzalez, Maxim Markevitch, Scott W. Randall, Christine Jones, and Dennis Zaritsky, A direct empirical proof of the existence of dark matter, Astrophys. J. **648**, L109 (2006).

[4] Massimo Persic, Paolo Salucci, and Fulvio Stel, The universal rotation curve of spiral galaxies: 1. The dark matter connection, Mon. Not. R. Astron. Soc. **281**, 27 (1996).

[5] Andrzej Drukier and Leo Stodolsky, Principles and applications of a neutral current detector for neutrino physics and astronomy, Phys. Rev. D **30**, 2295 (1984).

[6] Mark W. Goodman and Edward Witten, Detectability of certain dark matter candidates, Phys. Rev. D **31**, 3059 (1985).

[7] Marc Schumann, Direct detection of WIMP dark matter: Concepts and status, J. Phys. G **46**, 103003 (2019).

[8] Marco Battaglieri *et al.*, US cosmic visions: New ideas in dark matter 2017; Community report, Report No. FERMILAB-CONF-17-282-AE-PPD-T, 2017, arXiv: 1707.04591.

[9] Rouven Essig, Jeremy Mardon, and Tomer Volansky, Direct detection of sub-GeV dark matter, Phys. Rev. D **85**, 076007 (2012).

[10] Rouven Essig, Tomer Volansky, and Tien-Tien Yu, New constraints and prospects for sub-GeV dark matter scattering off electrons in Xenon, Phys. Rev. D **96**, 043017 (2017).

[11] P. Agnes *et al.* (DarkSide Collaboration), Constraints on sub-GeV dark-matter–electron scattering from the DarkSide-50 experiment, Phys. Rev. Lett. **121**, 111303 (2018).

[12] R. Agnese *et al.* (SuperCDMS Collaboration), First dark matter constraints from a SuperCDMS single-charge sensitive detector, Phys. Rev. Lett. **121**, 051301 (2018); **122**, 069901(E) (2019).

[13] E. Aprile *et al.* (XENON Collaboration), Light dark matter search with ionization signals in XENON1T, Phys. Rev. Lett. **123**, 251801 (2019).

[14] G. Cavoto, M. G. Betti, C. Mariani, F. Pandolfi, A. D. Polosa, I. Rago, and A. Ruocco, Carbon nanotubes as anisotropic target for dark matter, J. Phys. Conf. Ser. **1468**, 012232 (2020).

[15] Q. Arnaud *et al.* (EDELWEISS Collaboration), First germanium-based constraints on sub-MeV dark matter with the EDELWEISS experiment, Phys. Rev. Lett. **125**, 141301 (2020).

[16] Liron Barak *et al.* (SENSEI Collaboration), SENSEI: Direct-detection results on sub-GeV dark matter from a new skipper-CCD, Phys. Rev. Lett. **125**, 171802 (2020).

[17] E. Aprile *et al.* (XENON Collaboration), Search for new physics in electronic recoil data from XENONnT, Phys. Rev. Lett. **129**, 161805 (2022).

[18] Shuaijie Li *et al.* (PandaX Collaboration), Search for light dark matter with ionization signals in the PandaX-4T experiment, Phys. Rev. Lett. **130**, 261001 (2023).

[19] I. Arnquist *et al.* (DAMIC-M Collaboration), First constraints from DAMIC-M on sub-GeV dark-matter particles interacting with electrons, Phys. Rev. Lett. **130**, 171003 (2023).

[20] V. Zema *et al.*, Dark matter-electron scattering search using cryogenic light detectors, Phys. Rev. D **110**, 123012 (2024).

[21] Riccardo Catena, Timon Emken, Nicola A. Spaldin, and Walter Tarantino, Atomic responses to general dark matter-electron interactions, Phys. Rev. Res. **2**, 033195 (2020).

[22] Riccardo Catena, Timon Emken, Marek Matas, Nicola A. Spaldin, and Einar Urdshals, Crystal responses to general dark matter-electron interactions, Phys. Rev. Res. **3**, 033149 (2021).

[23] Riccardo Catena and Taylor R. Gray, Spin-1 thermal targets for dark matter searches at beam dump and fixed target experiments, J. Cosmol. Astropart. Phys. 11 (2023) 058.

[24] Riccardo Catena, Timon Emken, Marek Matas, Nicola A. Spaldin, and Einar Urdshals, Direct searches for general dark matter-electron interactions with graphene detectors: Part II. Sensitivity studies, Phys. Rev. Res. **5**, 043258 (2023).

[25] Riccardo Catena and Nicola Spaldin, Linear response theory for light dark matter-electron scattering in materials, Phys. Rev. Res. **6**, 033230 (2024).

[26] Einar Urdshals and Marek Matas, QEdark-EFT, Zenodo, 10.5281/zenodo.4739187 (2021).

[27] Paolo Giannozzi *et al.*, QUANTUM ESPRESSO: A modular and open-source software project for quantum, J. Phys. Condens. Matter **21**, 395502 (2009).

[28] Rouven Essig, Marivi Fernandez-Serra, Jeremy Mardon, Adrian Soto, Tomer Volansky, and Tien-Tien Yu, Direct detection of sub-GeV dark matter with semiconductor targets, J. High Energy Phys. 05 (2016) 046.

[29] D. Baxter *et al.*, Recommended conventions for reporting results from direct dark matter searches, Eur. Phys. J. C **81**, 907 (2021).

[30] B. G. Streetman and Sanjay Banerjee, *Solid State Electronic Devices* (Prentice Hall, Englewood Cliffs, NJ, 2005).

[31] C. A. Klein, Bandgap dependence and related features of radiation ionization energies in semiconductors, J. Appl. Phys. **39**, 2029 (1968).

[32] JiJi Fan, Matthew Reece, and Lian-Tao Wang, Non-relativistic effective theory of dark matter direct detection, J. Cosmol. Astropart. Phys. 11 (2010) 042.

[33] A. Liam Fitzpatrick, Wick Haxton, Emanuel Katz, Nicholas Lubbers, and Yiming Xu, The effective field theory of dark matter direct detection, J. Cosmol. Astropart. Phys. 02 (2013) 004.

[34] Abien Fred Agarap, Deep learning using rectified linear units (ReLU), arXiv:1803.08375.

[35] Martín Abadi *et al.*, TensorFlow: Large-scale machine learning on heterogeneous systems, software available from https://www.tensorflow.org/ (2015).

[36] Diederik P. Kingma and Jimmy Ba, Adam: A method for stochastic optimization, arXiv:1412.6980.

[37] K. Ramanathan and N. Kurinsky, Ionization yield in silicon for eV-scale electron-recoil processes, Phys. Rev. D **102**, 063026 (2020).

[38] https://github.com/urdshals/DEDD